

# Defect characterization of $\{10\bar{1}3\}$ GaN by electron microscopy

Cite as: J. Appl. Phys. **131**, 035705 (2022); doi: [10.1063/5.0077084](https://doi.org/10.1063/5.0077084)

Submitted: 30 October 2021 · Accepted: 31 December 2021 ·

Published Online: 19 January 2022



Gunnar Kusch,<sup>1,a)</sup>  Martin Frentrop,<sup>1</sup> Nan Hu,<sup>2</sup> Hiroshi Amano,<sup>2</sup> Rachel A. Oliver,<sup>1</sup>  and Markus Pristovsek<sup>2</sup>

## AFFILIATIONS

<sup>1</sup>Department of Materials Science and Metallurgy, Cambridge University, Cambridge CB3 0FS, United Kingdom

<sup>2</sup>Center for Integrated Research of Future Electronics, Institute for Materials and Systems for Sustainability, Nagoya University, Furo-cho, Chikusa-ku, Nagoya 464-8601, Japan

**Note:** This paper is part of the Special Topic on Defects in Semiconductors

**a)** Author to whom correspondence should be addressed: [gk419@cam.ac.uk](mailto:gk419@cam.ac.uk)

## ABSTRACT

Advances in obtaining untwinned  $(10\bar{1}3)$ -oriented semi-polar GaN enable a new crystal orientation for the growth of green and red LED structures. We present a scanning electron microscopy study that combines the structural characterization of electron channeling contrast imaging with the optical characterization of cathodoluminescence hyperspectral imaging on a  $(10\bar{1}3)$  GaN layer. An extensive defect analysis revealed that the dominant defects consist of basal plane stacking faults (BSFs), prismatic stacking faults, partial dislocations, and threading dislocations. With a defect density of about an order of magnitude lower than in comparable. The optical properties of the defects have been characterized from 10 to 320 K, showing BSF luminescence at room temperature indicating a reduced density of non-radiative recombination centers in the as-grown samples compared to established semi- and non-polar orientations. Our findings suggest that growth along  $(10\bar{1}3)$  has the potential for higher radiative efficiency than established semi-polar orientations.

Published under an exclusive license by AIP Publishing. <https://doi.org/10.1063/5.0077084>

## I. INTRODUCTION

III-nitride-based devices have already revolutionized ambient lighting, utilizing high efficiency  $\text{In}_x\text{Ga}_{1-x}\text{N}$ -based blue light-emitting diodes grown along the polar  $c$ -direction (with external quantum efficiencies approaching 85%<sup>1</sup>). However, this triumph has not been easily replicable in the green and red spectral regions, despite the nitride material system theoretically allowing for the bandgap to be tuned between 0.7 (InN) and 3.42 eV (GaN). One of the main limiting factors in achieving high efficiency devices in these regions lies in the strong inherent piezoelectric and spontaneous polarization fields, which cause the quantum confined Stark effect. This effect reduces the electron hole wave function overlap within the quantum wells (QWs), which, in turn, lowers the internal quantum efficiency.<sup>2–4</sup> The effect of these fields can be strongly reduced when the growth is performed on semi-polar planes and completely eliminated when the sample is grown on non-polar planes.<sup>5</sup>

One of the main challenges for the growth of semi-polar samples is the availability of suitable substrates. This is one of the main reasons as to why most published research on semi-polar

GaN focuses on the  $(11\bar{2}2)$  crystal orientation, which can be obtained easily and is phase-pure on  $m$ -plane sapphire.<sup>6,7</sup> Other GaN crystal orientations can be obtained as well on  $(1\bar{1}00)$  ( $m$ -plane) sapphire, i.e.,  $(10\bar{1}0)$  or  $(10\bar{1}3)$ .<sup>8,9</sup> Of these, the  $(10\bar{1}3)$  GaN orientation is the most dominant for the growth by hydride vapor phase epitaxy (HVPE), and the first semi-polar blue and green LEDs were demonstrated on it.<sup>10,11</sup> There was little follow up studying the growth along  $(10\bar{1}3)$ , despite the initial success, due to the majority of  $(10\bar{1}3)$  GaN growth on  $m$ -plane sapphire resulting in twinning as a result of the inherent bond symmetry. This, in turn, led to poor surface morphologies dominated by twin boundaries and high defect densities.<sup>11–13</sup> However, recently untwinned  $(10\bar{1}3)$  GaN layers have been achieved by patterned MOVPE<sup>14</sup> and HVPE growth,<sup>15,16</sup> as well as by directional sputtering on both  $(001)$  Si<sup>17,18</sup> and  $m$ -plane sapphire.<sup>9,19</sup> Using directional sputtering,  $(10\bar{1}3)$  oriented Al(Ga)N has been grown on  $m$ -plane sapphire as well.<sup>20</sup>

In an  $(0001)$  oriented LED, the polarization induced field across the QWs has the inverse sign compared to the electrical field from the pn-junction, whereas for semi-polar orientation with an

angle of  $\approx 50^\circ$  or higher [like (11 $\bar{2}2$ ) or (20 $\bar{1}1$ )], the polarization induced field has the same sign as the one from pn-junction.<sup>21</sup> The field of the pn-junction still persists in forward biased operation because the running voltage is below the GaN bandgap (e.g., 2.8 V for green LEDs). Therefore, the QWs from semi-polar orientations with more than  $\approx 40^\circ$  tilt from (0001) have the QWs tilted toward the p-GaN. Since the band offset is much lower for holes, the barrier becomes very thin. Hence, the hole states can extend far away from the QW, reducing overlap and increasing probability for non-radiative recombination. Therefore, one would like to have a small negative polarization field, with the (10 $\bar{1}3$ ) orientation being the closest achievable one<sup>21</sup> (see Fig. 1 in the [supplementary material](#) for calculation of the hole states in different hexagonal GaN crystal orientations).

To get a benefit from the highly confined holes with high overlap in the (10 $\bar{1}3$ ) orientation, the non-radiative recombination lifetime must be comparable to (0001). The non-radiative recombination lifetime is strongly dependent on the density and type of defects. Starting with point defects, which are not only controlling the conductivity (i.e., Si and Mg) but are also acting as carrier sinks, by offering alternative recombination pathways,<sup>22</sup> line defects [like perfect threading dislocations and partial dislocations (PDs)] can also act as non-radiative recombination centers,<sup>23</sup> lead to a spatially enhanced point defect incorporation,<sup>24</sup> or act as shunts, short circuiting entire devices.<sup>25</sup> Stacking faults [like basal plane stacking faults (BSFs) and prismatic stacking faults (PSFs)], on the other hand, were found to act as quantum wells in the III-nitrides, due to the introduction of the smaller bandgap cubic phase, locally changing the emission dynamics and providing localization sites for carriers.<sup>26–31</sup>

This work presents a study on the defect structure and properties of a single oriented semi-polar (10 $\bar{1}3$ ) GaN layer grown on an AlN/*m*-plane sapphire template. The GaN layer was intentionally Si-doped in order to prevent charging effects during the scanning electron microscopy based sample characterization. The defect structure and properties in the as-grown sample were analyzed using both electron channeling contrast imaging (ECCI) and temperature-dependent cathodoluminescence hyperspectral imaging (CL). ECCI is now an established alternative to transmission electron microscopy for analysis of the type and spatial distribution of crystal defects by electron diffraction. In ECCI, a semiconductor is imaged in an SEM at or close to a Bragg condition, with the disruption of the perfect crystals introduced by crystal defects producing a change in electron contrast.<sup>32,33</sup> Orienting the sample at a Bragg angle with respect to the electron beam is usually achieved by taking an electron channeling pattern (ECP) and then rotating and tilting the sample to bring a specific Kikuchi band, or channeling condition, into the center of the screen.<sup>33,34</sup> A different approach has been used by Zaefferer and Elhami,<sup>35</sup> who coupled ECC image acquisition with electron backscatter diffraction (EBSD) imaging. By determining the crystal orientation with EBSD measurements, Zaefferer and Elhami showed that they can calculate the position of the sample, within the instrument coordinate system, to obtain any desired diffraction condition for ECCI. When the diffraction condition and thus the **g** vector is known, one is even able to distinguish between the three different types of threading dislocations (edge,

mixed, screw), making the technique as powerful as transmission electron microscopy for defect identification, with the additional advantage that one can easily image large areas of the sample, building up significant statistics about their distribution.<sup>36</sup> The technique has previously been successfully used to investigate the defect structure in solar cells, metals, and (0001) (*c*-plane) GaN.<sup>34,37–40</sup> The first research on semi-polar GaN, investigating the widely used (11 $\bar{2}2$ ) orientation, was published by Naresh-Kumar *et al.*<sup>41</sup> They demonstrated the ability of ECCI on semi-polar samples to locate threading dislocation clustering as well as identify the presence of BSFs.

Complementary techniques to diffraction-based techniques like ECCI and TEM imaging for the identification of defects are luminescence-based techniques, in particular, CL, which offers the high spatial resolution necessary to map threading dislocations and stacking faults in semiconductor materials. The first work utilizing CL imaging for obtaining defect densities had already been performed in the early 1980s,<sup>42,43</sup> and studies investigating the luminescence behavior of threading dislocations go back just as far.<sup>44,45</sup> Stacking faults in the nitrides have been characterized by CL before, with particular research focus on the I<sub>1</sub>-type stacking faults.<sup>27</sup> CL is furthermore also capable of detecting optically active point defects utilizing their spectral signature.

The combination of both ECCI and CL is thus particularly suited for defect analysis, providing fast, non-destructive analysis of type, density, and impact on the carrier dynamics on a nanometer scale.

## II. EXPERIMENTAL

The semi-polar (10 $\bar{1}3$ ) GaN layer for this study was grown on a template based on directional sputtered AlN on *m*-plane sapphire.<sup>19</sup> The sputtered AlN was first overgrown with AlN in MOVPE and then with GaN in a two step process.<sup>9</sup> It was then stored for some time before the final Si-doped GaN layer was grown. The dopant was tetramethyl-silane, with a Si concentration of the top layer of  $\approx 5 \times 10^{18} \text{ cm}^{-3}$  in order to prevent charging effects during the scanning electron microscopy-based sample characterization. However, due to the low V/III ratio of 15, used to avoid roughening during the growth, the carrier concentration was in the upper  $10^{17} \text{ cm}^{-3}$ . The total sample thickness is 12  $\mu\text{m}$  with a 9  $\mu\text{m}$  thick template and 3  $\mu\text{m}$  GaN overgrowth.

Electron channeling contrast imaging (ECCI) was performed in a Hitachi SU-9000 scanning electron microscope (SEM). All ECC images were recorded with an acceleration voltage of 25 kV in backscatter geometry using a YAG backscatter electron detector.

Cathodoluminescence spectroscopy was performed in an Attolight Allalin 4027 Chronos dedicated CL scanning electron microscope. CL spectra and images were recorded with an iHR320 spectrometer with a focal length of 320 mm. Measurements were performed with a 600 l/mm grating blazed at 350 nm, or a 1200 l/mm grating blazed at 250 nm, and an Andor 1024 px charged coupled device. Grating and slit width were adjusted to provide the best compromise between resolution and intensity for each of the measurements. While most of the measurements were performed at 10 K with the above settings, a temperature-dependent

CL series from 10 to 320 K was measured with a 700  $\mu\text{m}$  slit width and the 1200 l/mm grating.

Both techniques were performed in top view geometry.

### III. RESULTS AND DISCUSSION

#### A. ECCI

ECCI measurements were performed in backscatter geometry. The rich sample morphology with characteristic surface undulations and the small final aperture of the utilized electron microscope (limiting the available angular range of the electron beam) made acquiring and indexing an electron channeling pattern (ECP) extremely challenging. Instead of selecting a channeling condition on the basis of an ECP, we tilted the sample in  $0.1^\circ$  steps and acquired a high resolution image at each step. In this way, we identified three different conditions, in the range from  $-7^\circ$  to  $+7^\circ$  sample tilt, in which contrast for the different defects was maximized. Changing the rotational axis of the sample was not possible with our setup due to limitations in the microscope geometry and the design of the used sample holder. While this way of conducting “blind” ECCI is significantly more time consuming than conventional ECCI using an ECP<sup>33,34</sup> or qualitative ECCI,<sup>35</sup> it does still carry all the advantages of the technique, namely, being a statistically significant, non-destructive, high resolution, correlative analysis of crystal defects and can be used independently of the microscope setup.

Three ECC images taken at the three diffraction conditions with highest contrast and recorded on the same area are shown in Fig. 1. We identified four main defect types within the sample, threading dislocations (TDs) [red circles in Fig. 1(c)], basal plane stacking faults (BSFs) [marked by green arrows in Fig. 1(a)], prismatic stacking faults (PSFs) [marked by blue arrows in Fig. 1(b)], and partial dislocations (PDs) [clearly visible with comet-like tails in Fig. 1(c), marked by orange arrows], terminating the line feature identified as a BSF. We identified these defects by means of comparing our acquired contrast with results published in the literature<sup>38,41,46</sup> as well as simple crystallographic considerations [i.e., a planar defect perpendicular to a BSF in (10 $\bar{1}$ 3) must be a PSF]. The alignment of the crystallographic relevant planes in the (10 $\bar{1}$ 3) orientation is shown in Fig. 3(a) in the [supplementary material](#).

Analyzing Fig. 1(a), we can, apart from PDs, clearly identify all the different defects. Although the contrast of threading dislocations is quite weak in Fig. 1(a), they can nonetheless be identified and the direction of their black-white contrast analyzed. BSFs [marked by green arrows in Fig. 1(a)] run along the diagonal length of the image, with strong black-white or white-black contrast perpendicular to their length. Three PSFs can be identified, two of which connect different BSFs in a stair-like arrangement in the bottom half of the image, while the other one appears to terminate a BSF.

The contrast due to scattering at the BSFs for the diffraction condition at  $3.9^\circ$  tilt [Fig. 1(b)] is opposite to the contrast observed for the diffraction condition at  $6.9^\circ$  tilt [Fig. 1(a)], with BSFs that showed a white-black contrast flipping to a black-white contrast and vice versa indicating a change in the sign of the diffraction vector. The threading dislocation contrast is quite faint at this diffraction condition, but a weak black-white contrast can still be

observed. However, no significant contrast change can be observed for PDs and PSFs when compared to Fig. 1(a).

The ECC image recorded at the diffraction condition at a tilt of  $-1.8^\circ$  [in Fig. 1(c)] reveals a fundamental change in the observable contrast. While the threading dislocation contrast is maximal, compared to the previously recorded images in (a) and (b), the SF contrast vanishes, with the SFs only visible as thin black lines, similar to the SE image in Fig. 1(d). Additionally, we can observe clear, bright lines, like comet tails, originating from some of the end points of the BSFs, indicating their origin to be from PDs.

Comparing the SE image shown in Fig. 1(d), we can clearly see that the contrast observed at dislocations and stacking faults in the BSE images is due to diffraction effects instead of surface morphology. While we are able to see features in the SE image at positions that we associate with dislocations and stacking faults, the contrast does not match the contrast observed in the BSE images. Additionally even with asymmetric surface pitting, we do not expect the contrast to flip when changing the tilt angle from  $6.9^\circ$  to  $3.9^\circ$ . Nonetheless, clear black lines and dots can be observed where BSFs, PSFs, TDs, and PDs are located. This is likely due to a local change in the surface morphology associated with defects, noticeable as a trough for SFs, and a pit for TDs and PDs. This morphology then produces a contrast visible in the SE image. Pits on top of dislocations are commonly found in AFM.<sup>47,48</sup>

By counting the defects and measuring the SF line length per area in the ECC images, we obtain a line defect density of  $(7 \pm 2) \times 10^8 \text{ cm}^{-2}$  (threading dislocations and partial dislocations) and a planar defect density of  $(3.5 \pm 1) \times 10^4 \text{ cm}^{-1}$  (basal plane and prismatic stacking faults).

Various studies reported in the literature have shown that ECCI analysis can also provide information on the threading dislocation type present in *c*-plane GaN.<sup>41,49,50</sup> This does usually involve knowledge of the exact diffraction condition, in order to analyze the change of the contrast in relation to the diffraction vector  $\mathbf{g}$ . But even without knowing the exact diffraction condition, a differentiation between pure edge and mixed/pure screw-type dislocations can be made by utilizing the change in ECCI contrast on the dislocations. This is due to the fact that the contrast of pure edge dislocations is independent of the diffraction vector  $\mathbf{g}$  and only depends on their Burgers vector  $\mathbf{b}$ .<sup>36,50</sup> The black-white contrast of edge dislocations originates from the tensile-compressive strain profile across the edge dislocation, and, thus, any change in the diffraction contrast that is different from a  $0^\circ$  or  $180^\circ$  flip indicates that the dislocation has a screw component.<sup>49</sup> This methodology has been tested thoroughly for *c*-plane GaN but has, to the best of our knowledge, not been studied theoretically or experimentally on semi-polar GaN. The main difference in comparison to *c*-plane GaN is the inclination angle of the threading dislocations when they intersect the surface. In semi-polar III-nitrides, threading dislocations are inclined to the sample surface, while for polar *c*-plane samples, threading dislocations are commonly found to intersect the *c*-plane surface at a  $90^\circ$  angle. However, other dislocation inclination angles have been found for *c*-plane AlGaN<sup>51,52</sup> and structures grown on epitaxial lateral overgrown (ELO) structures.<sup>53</sup> A change in the contrast flipping behavior of edge dislocations has not been reported for either sample structure<sup>54</sup> strongly indicating that the methodology works independent of the inclination angle

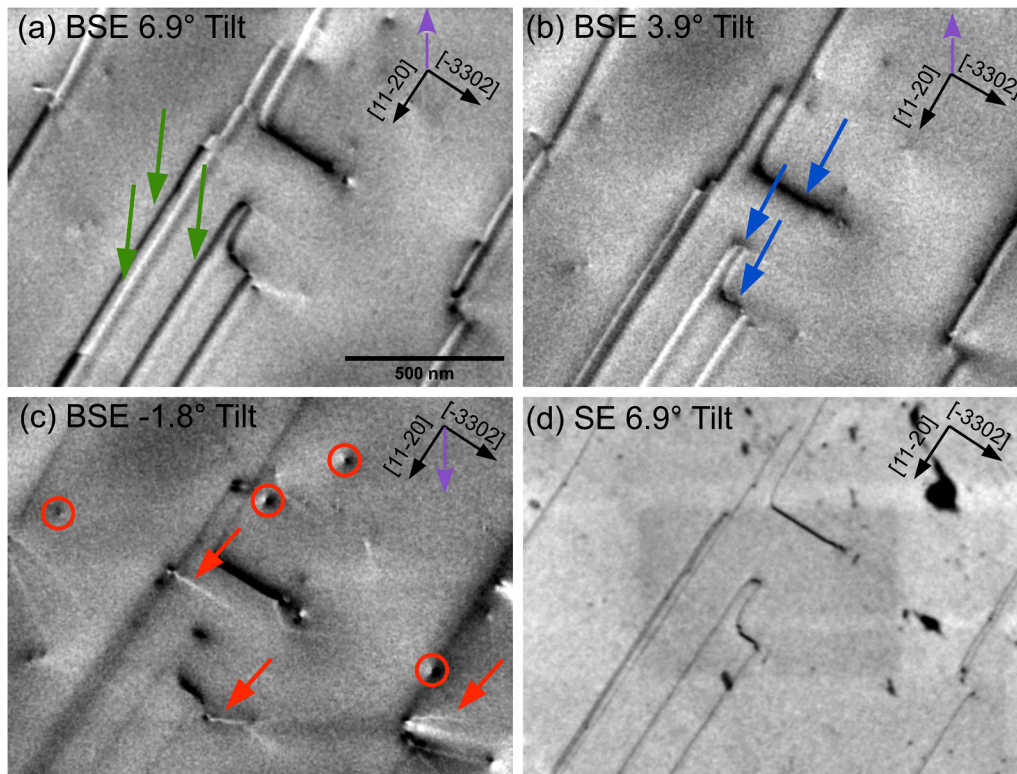


**FIG. 1.** Top view ECC images (a)–(c) taken at the same sample location for three different tilts. Images (a) and (b) clearly show black and white lines running diagonally through the image, which have been identified as BSFs (green arrows) and perpendicular to them PSFs (blue arrows). It is notable that from image (a) to (b), the contrast of the BSFs flips, while it nearly vanishes for the diffraction condition in (c). Contrast arising from threading dislocations (TDs) can be clearly seen in all three images [marked with red circles in (c)] and is highest in image (c). The SE image of the area is shown in (d). The scale bar in (a) applies to all images; the utilized tilt angle and signal type are written at the top. Crystallographic directions are marked in each image by black arrows, with the tilt direction marked by a purple arrow.

of the dislocation and hence can be used for semi-polar samples as well. Applying the same methodology to our semi-polar (10 $\bar{1}3$ ) oriented sample, we found that the main threading dislocation type present has a screw component and is therefore of screw/mixed nature. This is in contrast to *c*-plane GaN for which the main threading dislocation type was found to be edge-type dislocations, followed by mixed and screw types.<sup>36</sup> We would like to state that to improve the defect analysis and enhance its accuracy, a full **g** vector analysis should be performed, which will be subject to a future study.

The literature is sparse when analyzing stacking faults in GaN by ECCI, and no methodology to identify the stacking fault type by ECCI in GaN has been published yet. Despite these challenges, we are able to tentatively identify the stacking faults present in this sample. Wurtzite GaN can have four different types of stacking faults of the basal plane, three intrinsic ( $I_1$ ,  $I_2$ , and  $I_3$ ) and one extrinsic (E). The basal plane stacking faults can be differentiated by the number of breaches of the wurtzite stacking sequence ...AaBbAaBbAaBb... (with capital and non-capital for anion and cation respectively) or ...ABABABABABAB... (as a pair of cation and anion always share the same in-plane direction). The  $I_1$  BSF

corresponds to a single breach (...ABABCBCBCB...), the  $I_2$  (...ABABCACAC...) and the  $I_3$  BSFs (...ABABCBABA...) have two breaches, and the extrinsic (E) BSF has three breaches (...ABABCABAB...). Calculations by Wright<sup>55</sup> as well as Stampfl and Van de Walle<sup>56</sup> have shown that the  $I_1$  BSF has the lowest formation energy followed by the  $I_2$  BSF and then the E BSF. Based on these calculations, we tentatively ascribe all BSF contrast to  $I_1$ -type BSFs. The BSFs are marked by the earlier mentioned black-white or white-black contrast perpendicular to the length of the planar defect. This is analogous to the well documented fringe contrast observable in TEM<sup>57–59</sup> and matches the contrast reported for stacking faults in metals.<sup>38</sup> This contrast behavior is caused by the change of the phase shift ( $2 \times \pi \times g \times u$ , with the diffraction vector **g** and the displacement vector **u**) along the inclined basal plane stacking fault<sup>60</sup> and depends on the inclination angle ( $\approx 32.1^\circ$ ) and extinction distance in the material. It is notable, that some BSF lines show contrast inversion along the intersection line with the surface within the same diffraction condition, similar to observations made by Zakharov *et al.*<sup>57</sup> We attribute this behavior to imaging two different  $I_1$  BSFs with the opposite displacement vector **u**.



Most imaged BSFs are bounded by partial dislocations; these are particularly visible in Fig. 1(c), where they are marked by a “comet-like” tail (highlighted by orange arrows). These tails were previously observed by Picard *et al.*<sup>46</sup> who attributed them to the contrast from inclined dislocations. This is in agreement with our observations, as PDs terminating a BSF are parallel to the hexagonal *c*-plane and hence are tilted with respect to the surface in semi-polar samples. Partial dislocations are of particular interest, as they form the majority of line defects within this sample. They are, however, not the only way in which BSFs can be terminated. In the case where a BSF intersects a PSF, their partial dislocations react and form a stair-rod dislocation along their intersection line, with the Burgers vector being the sum of that of both partial dislocations. In wurtzite GaN, prismatic stacking faults can lie in either the (1120) or the (1100) prism planes, and we can clearly observe these types of defects in our sample [marked as blue arrows in Fig. 1(b)], either terminating a BSF or linking two BSFs, with a stair-rod dislocation at each intersection.<sup>57–59,61,62</sup> The type of PSF can be identified from the angle between the lines from the PSFs and the lines from BSFs at the (1013) surface. In our sample, these contrast lines run 90° to each other, which is [in case of the (1013) orientation] characteristic for (1120)-type PSFs, while the lines from (1010) PSFs would form an angle of about 64° with the BSF lines at the surface (as pole figure simulations reveal). An example for such an arrangement of a (1120) PSF and (0001) BSF with a stair-rod dislocation at the intersection line is illustrated in Fig. 3(b) in the [supplementary material](#). This observation is in agreement with theoretical calculations by Ruvimov, which predict that the (1120) PSF type in wurtzite GaN is energetically favorable having a lower formation energy.<sup>63</sup>

## B. Cathodoluminescence

In addition to ECC imaging, we also measured the optical properties of the sample using CL hyperspectral imaging. We acquired maps at various temperatures, ranging from 10 to 320 K. The results of the 10 K CL mapping are shown in Fig. 2.

Figure 2(a) shows the SE image acquired simultaneously with the hyperspectral CL image. We observe a large line feature in the center of the image and multiple thinner lines running across the length of the image, perpendicular to the larger feature (one of which is marked by a dashed red line). In addition to these line features, a number of pit-like features are apparent on the sample surface, some of which coincide with the end of one of the thin line features (one of which is marked by an orange circle). The general trend is similar to the observations made in the ECC images (Fig. 1), with the thin lines corresponding to BSFs, the large perpendicular line corresponding to a PSF, and the pits corresponding to partial and threading dislocations.

The mean CL spectrum shown in Fig. 2(b) shows two main peaks at 3.49 and 3.45 eV, with the 3.45 eV peak showing higher peak intensity, and one broad feature, likely consisting of multiple peaks at  $\approx 3.365$  eV. We identified these peaks as the NBE (3.49 eV), the emission from I<sub>1</sub> BSFs (3.45 eV), and a likely combination of luminescence from a PSF (3.38 eV) and possibly partial dislocations (3.36 eV).<sup>64</sup> The NBE signal is likely dominated by donor bound excitons at low temperature, but no exact

determination of the luminescence close to the bandgap has been done and we will be referring to it as NBE in the rest of the manuscript. While other planar defects like I<sub>2</sub> BSFs and E BSFs are possible to form too, the emission energy related to these defects is considerably lower (3.35 and 3.29 eV respectively),<sup>27</sup> and they are thus not further considered. The measured I<sub>1</sub> luminescence is on the high energy side of the reported values in the literature, with typical values ranging from 3.4 to 3.42 eV and energies up to 3.455 eV for Si-doped GaN.<sup>27–29,31,64,65</sup> The investigated sample was highly Si-doped, which, together with compressive thermal strain due to the growth on sapphire, explains why our observation lies on the high side of the range of values in literature. The energy differences between the I<sub>1</sub> peak and the PSF and PD peaks were reported to be 70 and 88 meV, respectively, underpinning our assignment of the broad peak in the mean spectrum being a convolution of a PSF peak at 3.38 eV and a peak potentially associated with PDs at 3.36 meV.<sup>64</sup>

Analyzing the spatial distribution of the luminescence intensity in the panchromatic CL image in Fig. 2(c), we find that the majority of pits (one marked by an orange circle) observed in the SE image act as non-radiative recombination centers, strongly reducing the local emission intensity. This is consistent with these pits originating from partial and perfect threading dislocations, which are known centers of non-radiative recombination in GaN.<sup>41,49</sup> We find that the large line feature visible in the SE image shows high luminescence intensity while the thinner line features (one marked with a dashed red line), perpendicular to the larger feature, are correlated with a drop in the intensity on one of their sides. In order to explore both the origin of the bright feature as well as the nature of the observed intensity drop close to the thin lines, we extract monochromatic slices from the hyperspectral data set at 3.49, 3.45, and 3.38 eV (the NBE, I<sub>1</sub> BSF, and PSF luminescence peaks, respectively).

Analyzing the NBE and I<sub>1</sub> BSF monochromatic emission intensity maps [Figs. 2(d) and 2(e), respectively], several observations can be made. First, both intensity maps are strongly anti-correlated, with the NBE generally showing high intensity in areas where the I<sub>1</sub> BSF emits weakly and vice versa (for example, at the location of the dashed red line, additionally see Fig. 2 in the [supplementary material](#)). Second, the exception to the anti-correlation is in areas related to the pits observed in the SE image and dark spots in the panchromatic CL, again underpinning their role as non-radiative defect centers. An additional exception is the large bright feature visible in the panchromatic CL image, which appears dark in both the NBE and I<sub>1</sub> BSF intensity maps, indicating that its origin lies in neither of these recombination paths. Third, it can be seen that both the NBE and the I<sub>1</sub> BSF luminescence intensity show a ramp-like behavior, with opposite signs, slowly increasing from their lowest intensity until reaching their respective maximum and then dropping, to increase again afterward (see Fig. 2 in the [supplementary material](#)). Finally, it can be seen that when comparing both of these monochromatic slices with the panchromatic CL, the recombination at I<sub>1</sub> BSFs is the dominant mechanism in this sample at 10 K, as the panchromatic CL intensity more strongly follows the I<sub>1</sub> BSF intensity than the NBE intensity. The direct competition between these two channels is likely also the cause for the ramp-like intensity increase of the I<sub>1</sub> BSF emission peak. As established, I<sub>1</sub> BSFs are at an angle of  $\approx 32.1^\circ$  to the surface, which means that the overlap between the excitation volume changes

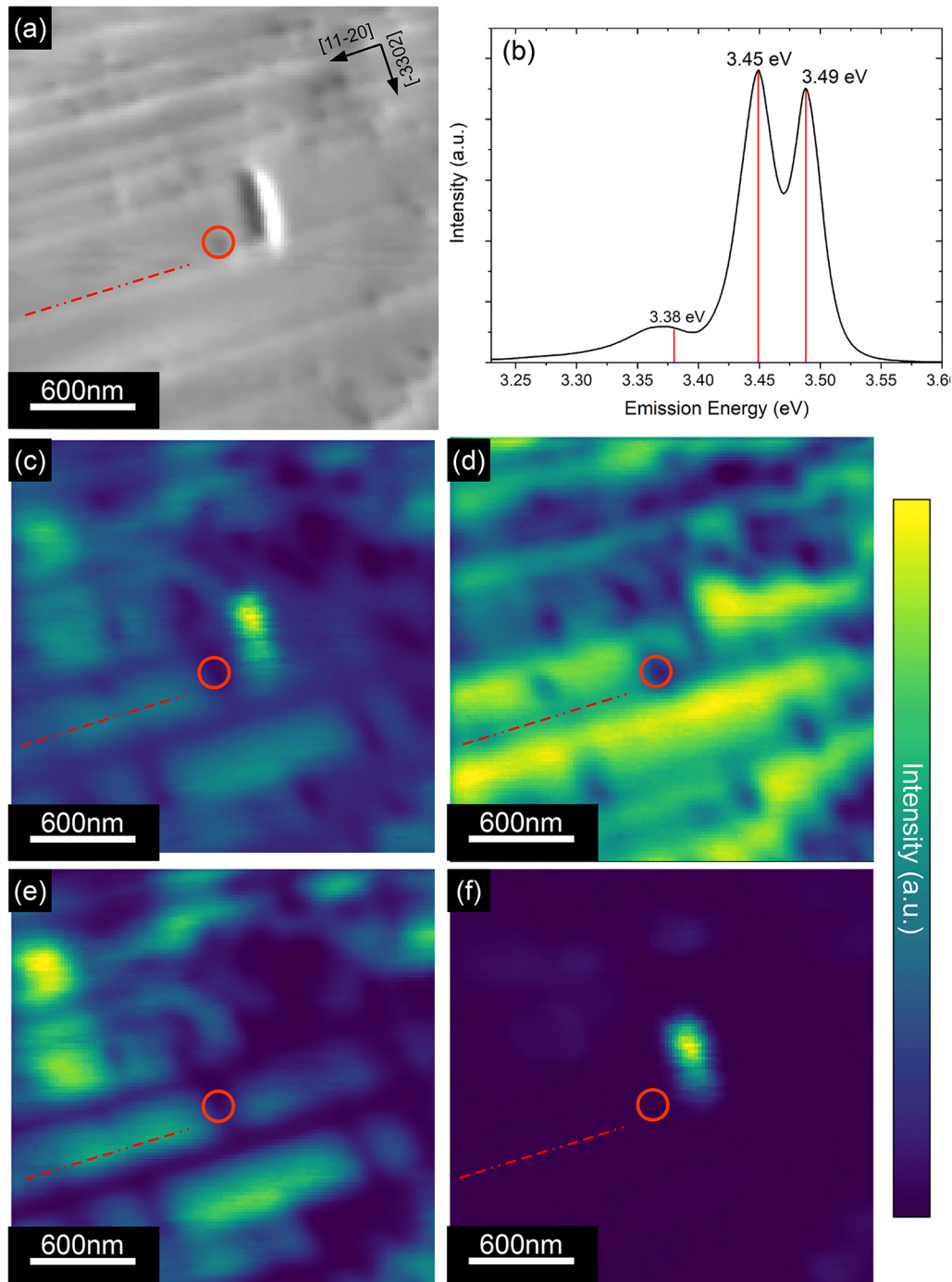


**FIG. 2.** SE image (a), mean CL spectrum (b), and panchromatic CL intensity (c) from the same area recorded at 10 K. Monochromatic images extracted from the hyperspectral data set showing the emission intensity at 3.49 (d), 3.45 (e), and 3.38 eV (f) for the NBE, the  $I_1$  BSF, and the PSF, respectively. The emission energies of the NBE (3.49 eV), the  $I_1$  BSF (3.45 eV), and the PSF (3.38 eV) are marked in the mean spectrum. The orange circle marks the location of a surface pit and the dashed line the position of an  $I_1$  BSF. Both the SE image as well as the CL images were taken in top view geometry.

differently depending upon the direction in which one moves away from the  $I_1$  BSF intersection with the surface. In one direction, the interaction volume follows the  $I_1$  BSF fault into the crystal, slowly reducing the overlap between interaction volume and  $I_1$  BSF, producing the observed slow increase in intensity, while in the other direction, a stronger drop in the overlap generates a faster drop in intensity. The resulting inhomogeneous intensity profile across a  $I_1$  BSF can be seen in Fig. 2 in the [supplementary material](#), with the measured profile being broadened compared to an ideal behavior due to the size of the interaction volume. The intensity behavior is analogous to the ECCI contrast, which shows an abrupt contrast change in one direction and a much slower change in contrast in the other.

Figure 2(f) shows the monochromatic intensity distribution at an emission energy of 3.38 eV, which we associate with PSF luminescence. We can clearly observe a highly localized region of intense emission, corresponding to the location of the large line feature, visible in the SE image [Fig. 2(a)]. The relative brightness of the PSF luminescence indicates that the PSF introduces, similar to a BSF, a local quantum well-like alteration to the GaN bandgap, increasing the electron-hole wave function overlap.

The 10 K measurements allowed us to clearly identify the different optical signals present in our samples and link them to our findings from the ECC images, confirming our previous analysis. While the  $I_1$  BSFs and the PSFs are acting as strong radiative carrier sinks at low temperature, understanding their behavior at room temperature is crucial for devices utilizing the semi-polar (10 $\bar{1}$ 3) crystal orientation. We performed temperature-dependent CL to track their luminescence properties to room temperature, heating the sample from 10 to 320 K, acquiring hyperspectral CL maps at set temperatures. We then proceeded to extract the spectra shown in Fig. 3 from the defect-free material, from an  $I_1$  BSF, and from a PSF.

The spectra from the defect-free material show an isolated GaN NBE peak [Fig. 3(a)], which redshifts by 70 meV from 3.49 to 3.42 eV, following the temperature-dependent bandgap variation, as described by the Varshni formula. The spectra taken from the  $I_1$  BSF show a similar behavior for the emission energy, following the same trend as the NBE luminescence. This is in stark contrast to the majority of reports found in the literature, where an S-shape-like behavior is reported for the temperature-dependent emission energy of the  $I_1$  BSF peak.<sup>30,66</sup> This S-shape behavior is characterized by a blueshift of the emission energy with increasing temperature, followed by a redshift. This trend is argued to be indicative of carrier localization within the investigated layer, with the blueshift being associated with a thermally activated redistribution process of carriers, changing the energetic carrier distribution from deeply localized states on to more shallow ones. The localization at an  $I_1$  BSF in GaN is attributed to three main factors, the lower bandgap of cubic GaN, the effect of the inherent piezoelectric fields on the resulting QW-like structure, and finally the spacing between different  $I_1$  BSFs.<sup>30,66,67</sup> Compared to values published by Forsberg *et al.*<sup>67</sup> ( $\approx 200$  Å), the spacing between the different BSFs is significantly larger in our sample, strongly reducing the hole confinement.<sup>67</sup> In addition to the large spacing between the BSFs, we also heavily Si-doped our sample, which was shown by Badcock *et al.*<sup>31</sup> to strongly reduce the S-shape behavior, with no S-shape being measurable by PL for a Si concentration at or above  $5 \times 10^{18} \text{ cm}^{-3}$ . This was attributed to the free electrons partially or

fully screening the inbuilt piezoelectric fields, which, in turn, leads to a reduction of the electron localization energy.<sup>31,67</sup> The large separation between BSFs in our experiment also means that we are likely only exciting a single, isolated BSF at a time, limiting the probed potential variations to a single BSF, while the experiments in the literature were performed by PL, analyzing the emission pattern when exciting large ensembles of BSFs. We thus attribute the lack of an S-shape behavior in the emission energy of our  $I_1$  BSFs to a combination of the large separation between BSFs in our sample as well as the high Si doping used.

We can furthermore observe that while the BSF luminescence dominates the low temperature spectra, the NBE to BSF intensity ratio increases with temperature, with the NBE emission becoming the dominant peak between 100 and 120 K. At 320 K the  $I_1$  BSF luminescence is only visible as a weak shoulder on the low energy side of the NBE peak. The exact nature of the relative intensity drop of the  $I_1$  BSF luminescence, i.e., activation of phonon assisted recombination channels localized at the BSF or electron de-localization, will be the subject of further study.

The PSF luminescence dependence on temperature in Fig. 3(c) reveals the same trend for the emission energy as for the other two peaks, with no sign of an S-shape to be found. The NBE to PSF luminescence intensity ratio notably shows the PSF as the dominant recombination channel up to a much higher temperature, with the NBE only dominating at a temperature above 240 K, where the PSF remains visible and clearly identifiable albeit with much lower intensity.

The results of the room temperature CL mapping are shown in Fig. 4. The SE image in Fig. 4(a) again clearly reveals both the 1D and 2D defects, informing us on the presence of both BSFs and PSFs as well as surface pits associated with line dislocations. Extracting monochromatic intensity maps at 3.42 (b), 3.37 (c), and 3.28 eV (d) for the NBE, the  $I_1$  BSF and the PSF luminescence, respectively, allows us to investigate the influence of each of the surface features on the room temperature spectrum.

Similar to the low temperature measurements, areas in the CL maps that spatially correlate with the presence of pits appear dark in the monochromatic CL images, again showing the nature of the threading dislocations associated with these pits as non-radiative defect centers. The NBE CL emission intensity map additionally shows reduced intensity in areas correlated with the BSF and PSF defects indicating the presence of competing recombination pathways (either radiative or non-radiative). Extracting a monochromatic intensity map at 3.37 eV reveals an intensity profile that correlates well with the thin lines in the SE image (identified as BSFs). We can clearly observe the same kind of behavior as measured at low temperature, namely, an increased intensity along the  $I_1$  BSF line. The resolution is generally not as good as at low temperature, partially due to both the NBE and the  $I_1$  BSF peaks merging with temperature as well as due to reduced carrier localization at the  $I_1$  BSF itself. The clear presence of BSF luminescence at room temperature is remarkable in itself. Most room temperature CL maps show a strongly reduced intensity at the location of BSFs, strongly indicating the presence of non-radiative recombination pathways (i.e., via point defects) at or close to BSFs.<sup>68–70</sup> The lack of such contrast in our study might tentatively be explained by a lower incorporation rate of point defects in (10 $\bar{1}$ 3). The



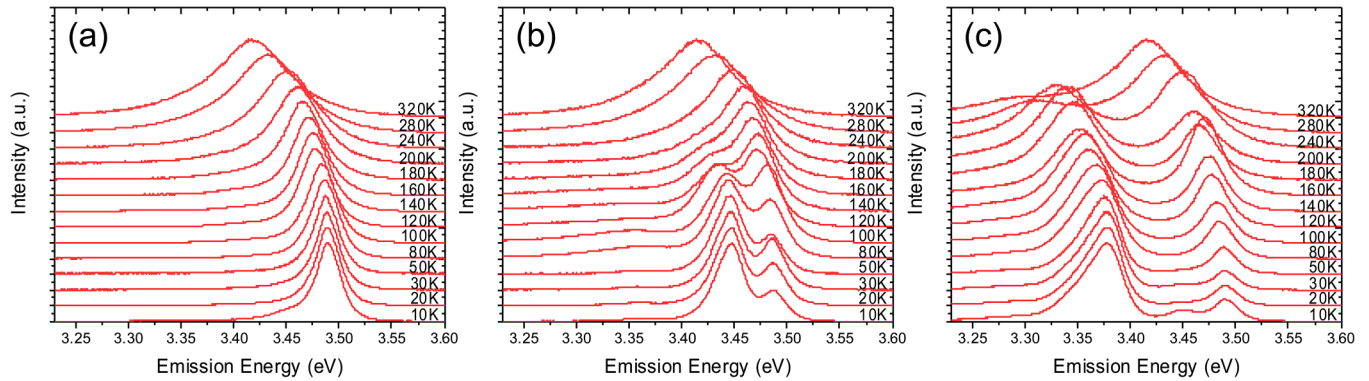


FIG. 3. Temperature-dependent CL spectra, extracted from defect-free material (a), an  $I_1$  BSF (b), and a PSF (c).

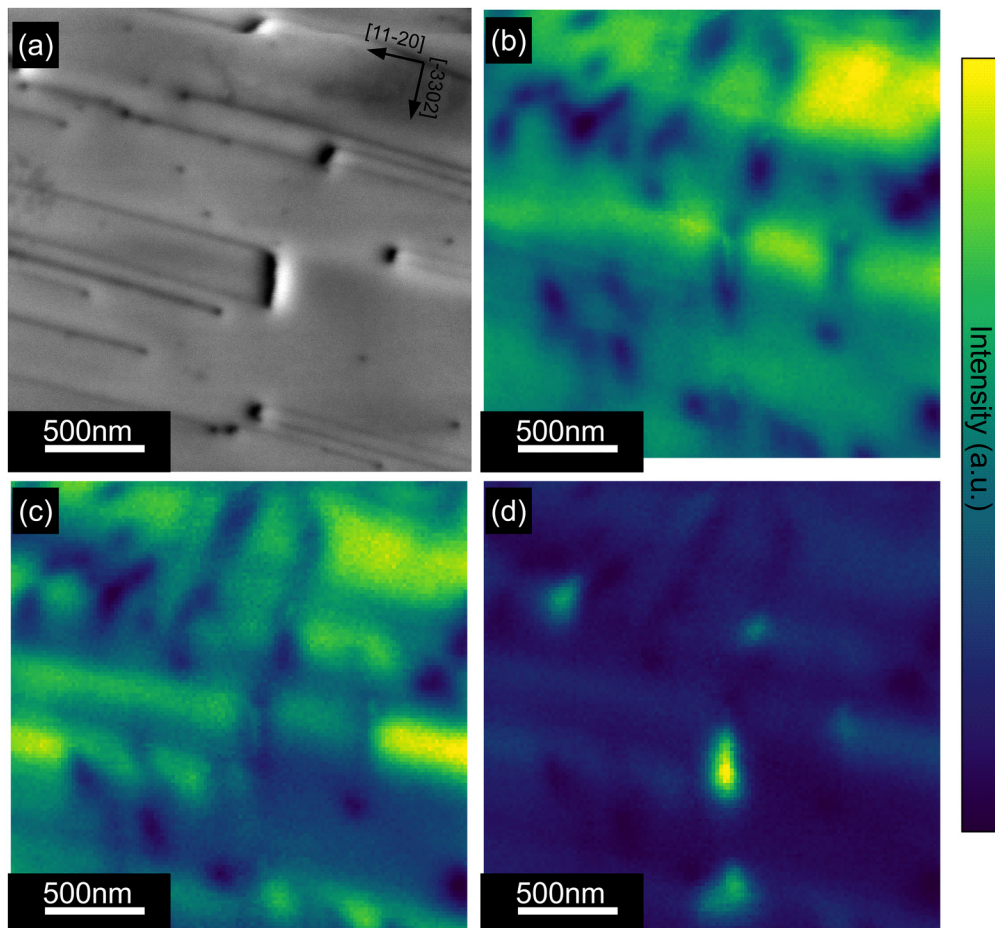


FIG. 4. SE image (a) and monochromatic images extracted from the hyperspectral data set recorded in the area shown in the SE. The monochromatic images are at 3.42 (b), 3.37 (c), and 3.28 eV (d) for the NBE, the  $I_1$  BSF, and the PSF, respectively. Both the SE image as well as the CL images were taken in top view geometry.



monochromatic luminescence intensity map at 3.28 eV [Fig. 4(d)] clearly shows the PSF luminescence, indicating that PSFs act as efficient carrier sinks even at room temperature.

#### IV. CONCLUSION

We have analyzed the optical and structural properties of a semi-polar (10 $\bar{1}$ 3) GaN layer by a combination of cathodoluminescence spectroscopy and electron channeling contrast imaging. We found that the dominant extended defects in the sample are partial dislocations as well as I<sub>1</sub> basal plane stacking faults, with threading dislocations and prismatic stacking faults also strongly influencing the sample properties. The defect density was found to be  $(7 \pm 2) \times 10^8 \text{ cm}^{-2}$  for line defects (threading and partial dislocations) and  $(3.5 \pm 1) \times 10^4 \text{ cm}^{-1}$  for planar defects. We additionally found, by ECCI contrast analysis, that the majority of threading dislocations are of mixed type. These defect densities are about an order of magnitude lower than those in the more studied (11 $\bar{2}$ 2) and (11 $\bar{2}$ 0) orientations, when grown directly on Al<sub>2</sub>O<sub>3</sub>.<sup>57,71–73</sup> This demonstrates a high suitability for utilizing the (10 $\bar{1}$ 3) orientation as a platform for the growth of semiconducting devices like green or red emitting LEDs. Our analysis of the optical properties of the crystal defects indicates that one of the main challenges for light-emitting devices will be the presence of prismatic stacking faults, which we have shown to be efficient carrier recombination centers even at room temperature.

#### SUPPLEMENTARY MATERIAL

See the [supplementary material](#) for band diagrams around an InGa<sub>0.15</sub>N QW for different crystal orientations as calculated using nextNano (Fig. 1); parameters used for the calculations shown in Fig. 1 (Table 1); a figure highlighting both the anti-correlation of the NBE CL intensity and the I<sub>1</sub> CL intensity and the different intensity behavior depending on the direction with which one moves over the I<sub>1</sub> BSF (Fig. 2); and sketch of the relative position of the *c*-plane (green), *m*-plane (yellow), and *a*-plane (blue) with respect to the (10–13) plane (white) (a) and position of the BSF and *a*-type PSF within a (10–13) oriented GaN crystal (Fig. 3).

#### ACKNOWLEDGMENTS

We acknowledge financial support from the EPSRC under Grant No. EP/R025193/1.

#### AUTHOR DECLARATIONS

##### Conflict of Interest

The authors declare no conflicts of interest.

#### DATA AVAILABILITY

The data that support the findings of this study are openly available in the University of Cambridge repository, Ref. 74.

#### REFERENCES

<sup>1</sup>M. Monavarian, A. Rashidi, and D. Feezell, “A decade of nonpolar and semipolar III-nitrides: A review of successes and challenges,” *Phys. Status Solidi A* **216**, 1800628 (2019).

- <sup>2</sup>D. A. B. Miller, D. S. Chemla, T. C. Damen, A. C. Gossard, W. Wiegmann, T. H. Wood, and C. A. Burrus, “Electric field dependence of optical absorption near the band gap of quantum-well structures,” *Phys. Rev. B* **32**, 1043–1060 (1985).
- <sup>3</sup>M. Leroux, N. Grandjean, M. Lüty, J. Massies, B. Gil, P. Lefebvre, and P. Bigenwald, “Quantum confined Stark effect due to built-in internal polarization fields in (Al, Ga)N/GaN quantum wells,” *Phys. Rev. B* **58**, R13371–R13374 (1998).
- <sup>4</sup>H. Amano, T. Takeuchi, S. Sota, H. Sakai, and I. Akasaki, “Structural and optical properties of nitride-based heterostructure and quantum-well structure,” *MRS Online Proc. Lib.* **449**, 1143–1150 (1996).
- <sup>5</sup>S.-H. Park, “Crystal orientation effects on electronic properties of wurtzite InGa<sub>0.15</sub>N/GaN quantum wells,” *J. Appl. Phys.* **91**, 9904–9908 (2002).
- <sup>6</sup>M. Pristovsek, M. Frentrup, Y. Han, and C. J. Humphreys, “Optimizing GaN (11 $\bar{2}$ 2) hetero-epitaxial templates grown on (10 $\bar{1}$ 0) sapphire,” *Phys. Status Solidi B* **253**, 61–66 (2016).
- <sup>7</sup>T. Wang, “Topical review: Development of overgrown semi-polar GaN for high efficiency green/yellow emission,” *Semicond. Sci. Technol.* **31**, 093003 (2016).
- <sup>8</sup>S. Ploch, M. Frentrup, T. Wernicke, M. Pristovsek, M. Weyers, and M. Kneissl, “Orientation control of GaN {11 $\bar{2}$ 2} and {10 $\bar{1}$ 3} grown on (10 $\bar{1}$ 0) sapphire by metal-organic vapor phase epitaxy,” *J. Cryst. Growth* **312**, 2171–2174 (2010).
- <sup>9</sup>N. Hu, D. V. Dinh, M. Pristovsek, Y. Honda, and H. Amano, “How to obtain metal-polar untwinned high-quality (10–13) GaN on *m*-plane sapphire,” *J. Cryst. Growth* **507**, 205–208 (2019).
- <sup>10</sup>A. Chakraborty, T. J. Baker, B. A. Haskell, F. Wu, J. S. Speck, S. P. DenBaars, S. Nakamura, and U. K. Mishra, “Milliwatt power blue InGa<sub>0.15</sub>N/GaN light-emitting diodes on semipolar GaN templates,” *Jpn. J. Appl. Phys.* **44**, L945–L947 (2005).
- <sup>11</sup>R. Sharma, P. M. Pattison, H. Masui, R. M. Farrell, T. J. Baker, B. A. Haskell, F. Wu, S. P. DenBaars, J. S. Speck, and S. Nakamura, “Demonstration of a semi-polar (10 $\bar{1}$ 3) InGa<sub>0.15</sub>N/GaN green light emitting diode,” *Appl. Phys. Lett.* **87**, 231110 (2005).
- <sup>12</sup>M. Frentrup, S. Ploch, M. Pristovsek, and M. Kneissl, “Crystal orientation of GaN layers on (10 $\bar{1}$ 0) *m*-plane sapphire,” *Phys. Status Solidi B* **248**, 583–587 (2011).
- <sup>13</sup>M. Jue, H. Yoon, H. Lee, S. Lee, and C. Kim, “A surface flattening mechanism of a heteroepitaxial film consisting of faceted non-flat top twins: [1103]-oriented GaN films grown on *m*-plane sapphire substrates,” *Appl. Phys. Lett.* **104**, 092110 (2014).
- <sup>14</sup>H. Yoon, M. Jue, D. Jang, and C. Kim, “Faceted growth of (1103)-oriented GaN domains on an SiO<sub>2</sub>-patterned *m*-plane sapphire substrate using polarity inversion,” *J. Appl. Crystallogr.* **50**, 30–35 (2017).
- <sup>15</sup>J. Yang, T. Wei, Z. Huo, Q. Hu, Y. Zhang, R. Duan, and J. Wang, “Hydride vapor phase epitaxy of high quality {10 $\bar{1}$ 3} semipolar GaN on *m*-plane sapphire coated with self-assembled SiO<sub>2</sub> nanospheres,” *J. Cryst. Growth* **387**, 101–105 (2014).
- <sup>16</sup>T. B. Wei, Q. Hu, R. F. Duan, X. C. Wei, J. K. Yang, J. X. Wang, Y. P. Zeng, G. H. Wang, and J. M. Li, “Hydride vapor phase epitaxy growth of semipolar (10 $\bar{1}$ 3)Ga<sub>0.15</sub>N on patterned *m*-plane sapphire,” *J. Electrochem. Soc.* **157**, H721 (2010).
- <sup>17</sup>H.-J. Lee, S.-Y. Bae, K. Lekhal, T. Mitsunari, A. Tamura, Y. Honda, and H. Amano, “Improved crystal quality of semipolar (10 $\bar{1}$ 3) GaN on Si(001) substrates using AlN/GaN superlattice interlayer,” *J. Cryst. Growth* **454**, 114–120 (2016).
- <sup>18</sup>T. Mitsunari, H. Lee, Y. Honda, and H. Amano, “Single-crystalline semipolar GaN on Si(001) using a directional sputtered AlN intermediate layer,” *J. Cryst. Growth* **431**, 60–63 (2015).
- <sup>19</sup>H. Nan, D. V. Dinh, M. Pristovsek, Y. Honda, and H. Amano, “Controlling the orientations of directional sputtered non- and semi-polar GaN/AlN layers,” *Jpn. J. Appl. Phys.* **58**, SC1044 (2019).
- <sup>20</sup>D. V. Dinh, N. Hu, H. Amano, Y. Honda, and M. Pristovsek, “Untwinned semipolar (10–13) Al<sub>x</sub>Ga<sub>1–x</sub>N layers grown on *m*-plane sapphire,” *Semicond. Sci. Technol.* **34**, 125012 (2019).

- <sup>21</sup>A. E. Romanov, T. J. Baker, S. Nakamura, and J. S. Speck, "Strain-induced polarization in wurtzite III-nitride semipolar layers," *J. Appl. Phys.* **100**, 023522 (2006).
- <sup>22</sup>A. M. Stoneham, "Non-radiative transitions in semiconductors," *Rep. Prog. Phys.* **44**, 1251–1295 (1981).
- <sup>23</sup>P. Petroff, R. Logan, and A. Savage, "Nonradiative recombination at dislocations in III-V compound semiconductors," *Phys. Rev. Lett.* **44**, 287 (1980).
- <sup>24</sup>G. Kusch, M. Nouf-Alleghiani, F. Mehnke, C. Kuhn, P. R. Edwards, T. Wernicke, A. Knauer, V. Kueller, G. Naresh-Kumar, M. Weyers, M. Kneissl, C. Trager-Cowan, and R. W. Martin, "Spatial clustering of defect luminescence centers in Si-doped low resistivity  $\text{Al}_{0.82}\text{Ga}_{0.18}\text{N}$ ," *Appl. Phys. Lett.* **107**, 072103 (2015).
- <sup>25</sup>M. Moseley, A. Allerman, M. Crawford, J. J. Wierer, M. Smith, and L. Biedermann, "Electrical current leakage and open-core threading dislocations in AlGaIn-based deep ultraviolet light-emitting diodes," *J. Appl. Phys.* **116**, 053104 (2014).
- <sup>26</sup>W. Rieger, R. Dimitrov, D. Brunner, E. Rohrer, O. Ambacher, and M. Stutzmann, "Defect-related optical transitions in GaN," *Phys. Rev. B* **54**, 17596–17602 (1996).
- <sup>27</sup>J. Lähnemann, U. Jahn, O. Brandt, T. Flissikowski, P. Dogan, and H. T. Grah, "Luminescence associated with stacking faults in GaN," *J. Phys. D: Appl. Phys.* **47**, 423001 (2014).
- <sup>28</sup>Y. T. Rebane, Y. G. Shreter, and M. Albrecht, "Stacking faults as quantum wells for excitons in wurtzite GaN," *Phys. Status Solidi A* **164**, 141–144 (1997).
- <sup>29</sup>P. Corfdir, J. Ristic, P. Lefebvre, T. Zhu, D. Martin, A. Dussaigne, J. D. Ganière, N. Grandjean, and B. Deveaud-Plédran, "Low-temperature time-resolved cathodoluminescence study of exciton dynamics involving basal stacking faults in a-plane GaN," *Appl. Phys. Lett.* **94**, 201115 (2009).
- <sup>30</sup>P. Corfdir, P. Lefebvre, J. Levrat, A. Dussaigne, J.-D. Ganière, D. Martin, J. Ristic, T. Zhu, N. Grandjean, and B. Deveaud-Plédran, "Exciton localization on basal stacking faults in a-plane epitaxial lateral overgrown GaN grown by hydride vapor phase epitaxy," *J. Appl. Phys.* **105**, 043102 (2009).
- <sup>31</sup>T. J. Badcock, M. J. Kappers, M. A. Moram, P. Dawson, and C. J. Humphreys, "Modification of carrier localization in basal-plane stacking faults: The effect of Si-doping in a-plane GaN," *Phys. Status Solidi B* **249**, 498–502 (2012).
- <sup>32</sup>G. R. Booker, A. M. B. Shaw, M. J. Whelan, and P. B. Hirsch, "Some comments on the interpretation of the 'kikuchi-like reflection patterns' observed by scanning electron microscopy," *Philos. Mag. A* **16**, 1185–1191 (1967).
- <sup>33</sup>A. J. Wilkinson and P. B. Hirsch, "Electron diffraction based techniques in scanning electron microscopy of bulk materials," *Micron* **28**, 279–308 (1997).
- <sup>34</sup>C. Trager-Cowan, F. Sweeney, P. W. Trimby, A. P. Day, A. Gholinia, N.-H. Schmidt, P. J. Parbrook, A. J. Wilkinson, and I. M. Watson, "Electron backscatter diffraction and electron channeling contrast imaging of tilt and dislocations in nitride thin films," *Phys. Rev. B* **75**, 085301 (2007).
- <sup>35</sup>S. Zaefferer and N.-N. Elhami, "Theory and application of electron channeling contrast imaging under controlled diffraction conditions," *Acta Mater.* **75**, 20–50 (2014).
- <sup>36</sup>G. Naresh-Kumar, B. Hourahine, P. R. Edwards, A. P. Day, A. Winkelmann, A. J. Wilkinson, P. J. Parbrook, G. England, and C. Trager-Cowan, "Rapid non-destructive analysis of threading dislocations in wurtzite materials using the scanning electron microscope," *Phys. Rev. Lett.* **108**, 135503 (2012).
- <sup>37</sup>K. N. Yaung, S. Kirnstoetter, J. Faucher, A. Gerger, A. Lochtefeld, A. Barnett, and M. L. Lee, "Threading dislocation density characterization in III-V photovoltaic materials by electron channeling contrast imaging," *J. Cryst. Growth* **453**, 65–70 (2016).
- <sup>38</sup>A. Weidner, S. Martin, V. Klemm, U. Martin, and H. Biermann, "Stacking faults in high-alloyed metastable austenitic cast steel observed by electron channeling contrast imaging," *Scr. Mater.* **64**, 513–516 (2011).
- <sup>39</sup>Y. N. Picard, J. D. Caldwell, M. E. Twigg, C. R. Eddy, M. A. Mastro, R. L. Henry, R. T. Holm, P. G. Neudeck, A. J. Trunek, and J. A. Powell, "Nondestructive analysis of threading dislocations in GaN by electron channeling contrast imaging," *Appl. Phys. Lett.* **91**, 094106 (2007).
- <sup>40</sup>T. J. Ruggles, J. I. Deitz, A. A. Allerman, C. B. Carter, and J. R. Michael, "Identification of star defects in gallium nitride with HREBSD and ECCI," *Microsc. Microanal.* **27**, 257–265 (2021).
- <sup>41</sup>G. Naresh-Kumar, D. Thomson, M. Nouf-Alleghiani, J. Bruckbauer, P. Edwards, B. Hourahine, R. Martin, and C. Trager-Cowan, "Electron channeling contrast imaging for III-nitride thin film structures," *Mater. Sci. Semicond. Process.* **47**, 44–50 (2016).
- <sup>42</sup>B. G. Yacobi and D. B. Holt, "Cathodoluminescence scanning electron microscopy of semiconductors," *J. Appl. Phys.* **59**, R1–R24 (1986).
- <sup>43</sup>M. Dupuy, "Cathodoluminescence studies of dislocations in semiconductors," *J. Phys. Colloq.* **44**, C4-277–C4-287 (1983).
- <sup>44</sup>P. Petroff and D. Lang, "A new spectroscopic technique for imaging the spatial distribution of nonradiative defects in a scanning transmission electron microscope," *Appl. Phys. Lett.* **31**, 60–62 (1977).
- <sup>45</sup>S. Pennycook, L. Brown, and A. Craven, "Observation of cathodoluminescence at single dislocations by stem," *Philos. Mag. A* **41**, 589–600 (1980).
- <sup>46</sup>Y. Picard, M. Liu, J. Lammatao, R. Kamaladasa, and M. De Graef, "Theory of dynamical electron channeling contrast images of near-surface crystal defects," *Ultramicroscopy* **146**, 71–78 (2014).
- <sup>47</sup>R. Oliver, M. Kappers, J. Sumner, R. Datta, and C. Humphreys, "Highlighting threading dislocations in MOVPE-grown GaN using an *in situ* treatment with  $\text{SiH}_4$  and  $\text{NH}_3$ ," *J. Cryst. Growth* **289**, 506–514 (2006).
- <sup>48</sup>M. A. Moram, C. F. Johnston, M. J. Kappers, and C. J. Humphreys, "Measuring dislocation densities in nonpolar *a*-plane GaN films using atomic force microscopy," *J. Phys. D: Appl. Phys.* **43**, 055303 (2010).
- <sup>49</sup>C. Trager-Cowan, A. Alasmari, W. Avis, J. Bruckbauer, P. R. Edwards, G. Ferenczi, B. Hourahine, A. Kotzai, S. Krausel, G. Kusch, R. W. Martin, R. McDermott, G. Naresh-Kumar, M. Nouf-Alleghiani, E. Pascal, D. Thomson, S. Vespucci, M. D. Smith, P. J. Parbrook, J. Enslin, F. Mehnke, C. Kuhn, T. Wernicke, M. Kneissl, S. Hagedorn, A. Knauer, S. Walde, M. Weyers, P.-M. Coulon, P. A. Shields, J. Bai, Y. Gong, L. Jiu, Y. Zhang, R. M. Smith, T. Wang, and A. Winkelmann, "Structural and luminescence imaging and characterisation of semiconductors in the scanning electron microscope," *Semicond. Sci. Technol.* **35**, 054001 (2020).
- <sup>50</sup>Y. Picard, M. Twigg, J. Caldwell, C. Eddy, M. Mastro, and R. Holm, "Resolving the Burgers vector for individual GaN dislocations by electron channeling contrast imaging," *Scr. Mater.* **61**, 773–776 (2009).
- <sup>51</sup>D. M. Follstaedt, S. R. Lee, P. P. Provencio, A. A. Allerman, J. A. Floro, and M. H. Crawford, "Relaxation of compressively-strained AlGaIn by inclined threading dislocations," *Appl. Phys. Lett.* **87**, 121112 (2005).
- <sup>52</sup>K. Forghani, L. Schade, U. T. Schwarz, F. Lipski, O. Klein, U. Kaiser, and F. Scholz, "Strain and defects in Si-doped (Al)GaN epitaxial layers," *J. Appl. Phys.* **112**, 093102 (2012).
- <sup>53</sup>A. Mogilatenko, V. Küller, A. Knauer, J. Jeschke, U. Zeimer, M. Weyers, and G. Tränkle, "Defect analysis in AlGaIn layers on AlN templates obtained by epitaxial lateral overgrowth," *J. Cryst. Growth* **402**, 222–229 (2014).
- <sup>54</sup>C. Trager-Cowan, A. Alasmari, W. Avis, J. Bruckbauer, P. R. Edwards, B. Hourahine, S. Krausel, G. Kusch, R. Johnston, G. Naresh-Kumar, R. W. Martin, M. Nouf-Alleghiani, E. Pascal, L. Spasevski, D. Thomson, S. Vespucci, P. J. Parbrook, M. D. Smith, J. Enslin, F. Mehnke, M. Kneissl, C. Kuhn, T. Wernicke, S. Hagedorn, A. Knauer, V. Kueller, S. Walde, M. Weyers, P.-M. Coulon, P. A. Shields, Y. Zhang, L. Jiu, Y. Gong, R. M. Smith, T. Wang, and A. Winkelmann, "Scanning electron microscopy as a flexible technique for investigating the properties of UV-emitting nitride semiconductor thin films," *Photon. Res.* **7**, B73–B82 (2019).
- <sup>55</sup>A. F. Wright, "Basal-plane stacking faults and polymorphism in AlN, GaN, and InN," *J. Appl. Phys.* **82**, 5259–5261 (1997).
- <sup>56</sup>C. Stampfl and C. G. Van de Walle, "Energetics and electronic structure of stacking faults in AlN, GaN, and InN," *Phys. Rev. B* **57**, R15052–R15055 (1998).
- <sup>57</sup>D. N. Zakharov, Z. Liliental-Weber, B. Wagner, Z. J. Reitmeier, E. A. Preble, and R. F. Davis, "Structural tem study of nonpolar *a*-plane gallium nitride grown on (11 $\bar{2}$ 0) 4H-SiC by organometallic vapor phase epitaxy," *Phys. Rev. B* **71**, 235334 (2005).

- <sup>58</sup>H. Blank, P. Delavignette, R. Gevers, and S. Amelinckx, "Fault structures in wurtzite," *Phys. Status Solidi B* **7**, 747–764 (1964).
- <sup>59</sup>C. M. Drum, "Intersecting faults on basal and prismatic planes in aluminium nitride," *Philos. Mag. A* **11**, 313–334 (1965).
- <sup>60</sup>H. Kriaa, A. Guitton, and N. Maloufi, "Modelling electron channeling contrast intensity of stacking fault and twin boundary using crystal thickness effect," *Materials* **14**, 1696 (2021).
- <sup>61</sup>J. Bai, X. Huang, M. Dudley, B. Wagner, R. F. Davis, L. Wu, E. Sutter, Y. Zhu, and B. J. Skromme, "Intersecting basal plane and prismatic stacking fault structures and their formation mechanisms in GaN," *J. Appl. Phys.* **98**, 063510 (2005).
- <sup>62</sup>Y.-L. Hu, S. Krämer, P. T. Fini, and J. S. Speck, "Atomic structure of prismatic stacking faults in nonpolar a-plane GaN epitaxial layers," *Appl. Phys. Lett.* **101**, 112102 (2012).
- <sup>63</sup>S. Ruvimov, "Defect engineering in III-nitrides epitaxial systems," in *III-Nitride Semiconductors: Electrical, Structural and Defects Properties*, edited by O. Manasreh (Elsevier, Amsterdam, 2000), Chap. 3, pp. 51–75.
- <sup>64</sup>R. Liu, A. Bell, F. A. Ponce, C. Q. Chen, J. W. Yang, and M. A. Khan, "Luminescence from stacking faults in gallium nitride," *Appl. Phys. Lett.* **86**, 021908 (2005).
- <sup>65</sup>K. Furusawa, Y. Ishikawa, H. Ikeda, K. Fujito, and S. F. Chichibu, "Local excitation and emission dynamics of an isolated single basal-plane stacking-fault in GaN studied by spatio-time-resolved cathodoluminescence," *Jpn. J. Appl. Phys.* **54**, 030303 (2015).
- <sup>66</sup>P. P. Paskov, R. Schifano, B. Monemar, T. Paskova, S. Figge, and D. Hommel, "Emission properties of a-plane GaN grown by metal-organic chemical-vapor deposition," *J. Appl. Phys.* **98**, 093519 (2005).
- <sup>67</sup>M. Forsberg, A. Serban, I. Poenaru, C.-L. Hsiao, M. Junaid, J. Birch, and G. Pozina, "Stacking fault related luminescence in GaN nanorods," *Nanotechnology* **26**, 355203 (2015).
- <sup>68</sup>J. S. Speck and S. F. Chichibu, "Nonpolar and semipolar group III nitride-based materials," *MRS Bull.* **34**, 304–312 (2009).
- <sup>69</sup>F. Scholz, "Semipolar GaN grown on foreign substrates: A review," *Semicond. Sci. Technol.* **27**, 024002 (2012).
- <sup>70</sup>J. Bruckbauer, Y. Gong, L. Jiu, M. J. Wallace, A. Ipsen, S. Bauer, R. Müller, J. Bai, K. Thonke, T. Wang, C. Trager-Cowan, and R. W. Martin, "Influence of micro-patterning of the growth template on defect reduction and optical properties of non-polar (11 $\bar{2}$ 0) GaN," *J. Phys. D: Appl. Phys.* **54**, 025107 (2020).
- <sup>71</sup>M. Pristovsek, M. Frentrup, Y. Han, and C. J. Humphreys, "Optimising GaN (11 $\bar{2}$ 2) heteroepitaxial templates grown on (10 $\bar{1}$ 0) Al<sub>2</sub>O<sub>3</sub>," *Phys. Status Solidi B* **253**, 61–66 (2016).
- <sup>72</sup>M. Pristovsek, M. Frentrup, T. Zhu, G. Kusch, and C. J. Humphreys, "X-ray characterisation of the basal stacking fault densities of (11-20) GaN," *CrystEngComm* **23**, 6059–6069 (2021).
- <sup>73</sup>J. Smalc-Koziorowska, G. Tsiakatouras, A. Lotsari, A. Georgakilas, and G. P. Dimitrakopoulos, "The defect character of GaN growth on r-plane sapphire," *J. Appl. Phys.* **107**, 073525 (2010).
- <sup>74</sup>N. Amano-Patiño, E. Faraglia, C. Giannitsarou, and Z. Hasna, (2011). "The unequal effects of Covid-19 on economists' research productivity," *Faculty of Economics*, University of Cambridge.